Dalton Transactions

ROYAL SOCIETY OF CHEMISTRY

PAPER

View Article Online
View Journal | View Issue

Cite this: *Dalton Trans.*, 2021, **50**, 7554

Mixed functionalization strategy on indium-organic framework for multiple ion detection and H_2O_2 turn-on sensing†

Xin Jiang, Ruiqing Fan, * Xuesong Zhou, Ke Zhu, Tiancheng Sun, Xubin Zheng, Kai Xing, Wei Chen and Yulin Yang *

A special functional group mediated functionalization platform is introduced as a new and versatile platform tool to improve the fluorescence detection performance of metal–organic frameworks (MOF). The creation of a mixed-functionalization strategy on a MOF realizes the high sensitivity detection of heavy metal ions, anions and small molecules. In this work, we have first reported a novel amino functionalized 3D indium MOF $[In(BDC\text{-}NH_2)(OH)]_n$ (**In1-NH$_2$**) which not only has an excellent fluorescent characteristic but also shows highly sensitive identification of Fe^{3+}, Cu^{2+}, Pb^{2+} and ClO^- in water with broad linear ranges and short response times. Subsequently, based on the remaining amino group site of **In1-NH$_2$**, a post-synthetic modification strategy is utilized to introduce an active boronic acid group for hydrogen peroxide detection. The obtained **PBA-In1** exhibits an efficient sensing performance for hydrogen peroxide with an LOD of 0.42 μM. Given this, **PBA-In1** is expected to become an effective probe to monitor the formation of metabolites in humans. **In1-NH$_2$** successfully achieves multiple ion detection and the **PBA-In1** sensing platform with boronic acid functionalization may have good application prospects in biochemical research in the future.

Received 18th March 2021,
Accepted 23rd April 2021

DOI: 10.1039/d1dt00889g

rsc.li/dalton

Introduction

As the source of life, water is indispensable to human beings and water quality is closely related to human health. Thus, water quality monitoring is an eternal topic. The harm to human health caused by heavy metal ions, the most common pollutants in water, cannot be ignored and has caught the attention of the international community.[1–5] For example, excess intake of Fe^{3+} in the human body can cause damage to the heart and liver, which can lead to iron poisoning or cancer;[6–9] excessive Cu^{2+} may lead to recessive genetic congenital diseases, as well as liver and kidney disfunction;[10–13] Pb^{2+} is also an accumulative toxicant that has a detrimental effect on the hematopoietic system and nervous system, causing various diseases.[14–16] On the other hand, various anions also occupy important roles in the water environment.[17] Among them, hypochlorite (ClO^-) is widely used as a disinfectant for water treatment and its residual content should be strictly controlled. A large amount of residual ClO^- in water may be transformed into highly toxic substances, while inadequate ClO^- cannot provide good disinfection.[18–20] Therefore, it is of great significance to develop a probe that performs the detection of heavy metal ions and ClO^- in water.

Hydrogen peroxide (H_2O_2) is a vital reactive oxygen species (ROS) in living systems and participates in a variety of cellular activities, such as protein folding and cell migration.[21–24] As a common byproduct of cellular metabolism, the abnormal accumulation of H_2O_2 in cells may lead to intracellular oxidative stress,[25] which is associated with the initiation of many diseases.[26,27] Thus, it is of great importance to develop a sensitive sensor to detect H_2O_2 for human health. In recent years, the sensors based on boronic acid has attracted widespread attention.[28] The boronic acid group is capable of recognizing H_2O_2 as well as substances with diol structures.[29,30] For example, Dickinson *et al.* presented a series of monoboronate probes that respond to H_2O_2.[31] Although many materials have been reported to detect H_2O_2 using the boronic acid group,[32,33] the low surface area and insufficient functional groups of most materials limit their detection abilities. Therefore, the development of new materials with rich boronic acid active sites to detect H_2O_2 is of great importance. Up to now, the monitoring

MIIT Key Laboratory of Critical Materials Technology for New Energy Conversion and Storage, School of Chemistry and Chemical Engineering, Harbin Institute of Technology, P. R. China. E-mail: fanruiqing@hit.edu.cn, ylyang@hit.edu.cn; Fax: +86-451-86418270

†Electronic supplementary information (ESI) available: PXRD patterns, fluorescence spectras and additional experimental details. CCDC 2008844. For ESI and crystallographic data in CIF or other electronic format see DOI: 10.1039/d1dt00889g

technologies for cations, anions and molecules have mainly including high performance liquid chromatography (HPLC),[34] electrochemical detection,[35,36] colorimetry,[37,38] and fluorescence method.[39–42] Compared with other approaches, the fluorescence method exhibits the significant advantages of simplicity, low cost and short response time,[43–46] ideal for applications in substance detection.

As novel multi-functional materials, metal–organic frameworks (MOFs) have exhibited many advantages, such as stable frame structure, high specific surface area, adjustable porosity and diverse functional sites,[47] presenting potential application prospects in the fields of catalysis,[48] batteries,[49] gas storage,[50] drug loading[51] and especially fluorescence probes.[52] For different practical application requirements, through the combination of central metal ions and functional organic ligands, various MOFs with unique functional sites can be designed and synthesized. However, MOFs directly synthesized by hydrothermal method usually cannot meet these practical application requirements;[53,54] the limitations of direct synthesis methods and the increasing demand for more complex MOFs have promoted remarkable progress in post-synthetic modification (PSM) reactions.[55] Thus, it is important that functional sites can be effectively introduced into MOFs through the PSM method, further expanding the application of such materials.

As a high-valence metal ion, indium is an ideal choice to construct MOFs with high chemical stability.[56] In this study, we report a novel 3D In(III)-based MOF by introducing a new amino functionalized ligand, $[In(BDC\text{-}NH_2)(OH)]_n$ (**In1-NH$_2$**), where $H_2BDC\text{-}NH_2$ = 2-aminoterephthalic acid. Notably, the introduced uncoordinated amino groups endow the framework with excellent fluorescence performance and provide the ability to detect heavy metal ions as well as ClO^-. The obtained fluorescence probe shows excellent quenching performance in the detection of Fe^{3+}, Cu^{2+} and Pb^{2+} and also has a good effect in the detection of ClO^-. **In1-NH$_2$** is an excellent fluorescent probe that can be used for water quality monitoring. At the same time, using a mixed-functionalization strategy, a PSM strategy with 4-carboxyl phenylboronic acid (CPBA) is designed to generate a phenylboronic acid-functionalized composite material (**PBA-In1**) to provide a suitable H_2O_2-sensing platform. Consequently, the prepared **PBA-In1** shows an obvious fluorescence turn-on response for H_2O_2 with a low limit of detection (LOD) of 0.42 μM. The powerful sensing performances of both **In1-NH$_2$** and **PBA-In1** make them promising candidates for water quality monitoring and biomarker detection (Scheme 1).

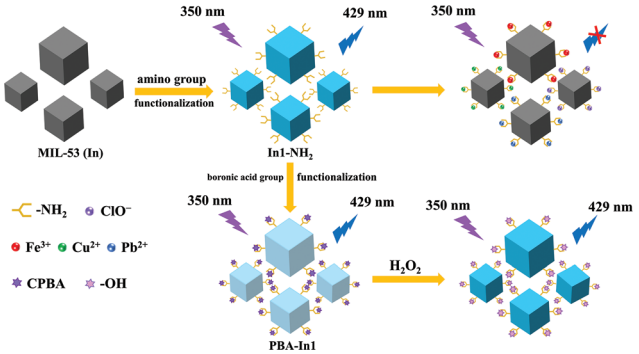

Scheme 1 The schematic for the detection of heavy metal ions and ClO^- by **In1-NH$_2$** and the detection of H_2O_2 by **PBA-In1**.

Results and discussion

Structural description of In1-NH$_2$

Herein, we report the 3D indium-based MOF $[In(BDC\text{-}NH_2)(OH)]_n$ whose single crystal X-ray diffraction analysis illustrates that it belongs to the orthorhombic system and the *Imma* space group. In each asymmetric structural unit, the unit cell possesses a quarter of the In^{3+}, a quarter of the $NH_2\text{-}BDC^{2-}$ and a quarter of the coordinated hydroxyl (Fig. S1a†). In addition, each In^{3+} coordinates with six oxygen atoms (four from four different $NH_2\text{-}BDC^{2-}$ ligands and two from coordinated hydroxyls), forming an octahedral geometry as shown in Fig. S1b.† The completely deprotonated $NH_2\text{-}BDC^{2-}$ coordinates with four In^{3+} ions through the $\mu_4\text{–}\eta_o^1\text{:}\eta_o^1\text{:}\eta_o^1\text{:}\eta_o^1$-bridging mode. Furthermore, adjacent In^{3+} ions are linked by the hydroxyl oxygen atoms along the *b* axis to form 1D chains (Fig. S1c†) and these 1D chains interconnect through the $NH_2\text{-}BDC^{2-}$ ligands to form a 3D frame structure with obvious 1D channels (Fig. 1a and c). The rhombic window size of the 1D channels is 12.05 Å × 18.26 Å (Fig. 1b) and, according to PLATON, the total solvent-accessible volume in the framework of **In1-NH$_2$** is estimated to be 44.5% of its unit cell. The appro-

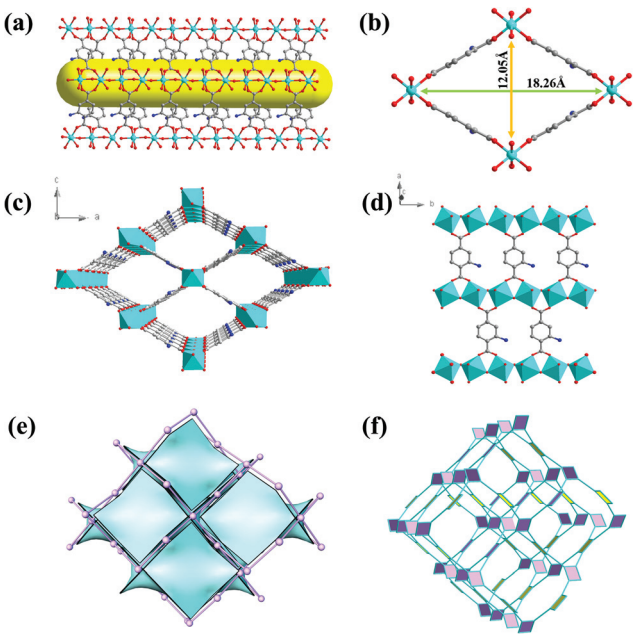

Fig. 1 Crystal structure of **In1-NH$_2$**: (a) the 1D channel of **In1-NH$_2$**; (b) the 1D rhombic channels of about 12.05 Å × 18.26 Å; (c) the 3D structure of **In1-NH$_2$**; (d) view perpendicular to the pore system; (e) the natural tiling of **In1-NH$_2$**; (f) the view of the ***lvt*** topology network of **In1-NH$_2$**, in which the yellow quadrilateral represents 4-connected ligands and the purple one represents the 4-connected In^{3+} ion.

priate porosity and remaining amino groups (Fig. 1d) are believed to provide accessible affinity sites to some heavy metal ions as well as reactive sites for the PSM method. The topological analysis suggests a 4,4-connected ***lvt*** network (Fig. 1e and f). The details of the crystal structure parameters are provided in Table S1† and selected bond angles and bond lengths are listed in Table S2.†

Characterization of In1-NH_2 and PBA-In1

The powder X-ray diffraction (PXRD) analysis of **In1-NH_2** indicates that the diffraction peaks of the actual pattern precisely match those observed in the simulated pattern, which proves the high purity of the as-synthesized **In1-NH_2** samples (Fig. 2a). It is well known that some MOF crystals are unstable in aqueous solution, so investigation of the water stability of **In1-NH_2** is necessary to meet the needs of practical applications. In this case, fresh crystal samples of **In1-NH_2** were treated by immersion in water for a week and the PXRD of treated samples closely matched those of the untreated samples, indicating that the crystallinity of **In1-NH_2** was not affected (Fig. 2b). In addition, the PXRD patterns of **In1-NH_2** in different aqueous solutions with various pH values (3–11) were also recorded. No obvious changes can be observed, suggesting that **In1-NH_2** has high chemical resistance, which fulfills a good prerequisite for its detection applications.

Subsequently, the thermal stability of **In1-NH_2** was studied *via* thermal gravimetric analysis (TGA), which was performed from 40 °C to 750 °C under a flow of air. The corresponding curve is recorded in Fig. 2d. Primarily, the first weight loss (3.31%) can be ascribed to the removal of free H_2O molecules in the channel from room temperature to 233 °C, while the coordinated hydroxyl left in the range of 233 °C–340 °C. Finally, the third rapid weight loss was caused by the decomposition of the NH_2-BDC^{2-} ligands from 340 °C to 470 °C, corresponding to the collapse of the **In1-NH_2** framework. After further heating, the weight loss of the TGA curve remains unchanged. The residual weight of **In1-NH_2** is 44.25%, corresponding to the theoretical calculation result (In_2O_3 is 44.64%). In addition, fluorescence emission is a vital prerequisite for a fluorescent detector. As shown in Fig. 2c, **In1-NH_2** shows strong blue emission under UV irradiation. The fluorescence emission peak of **In1-NH_2** is located at 429 nm (λ_{ex} = 350 nm) and was ascribed to the intra-ligand $\pi^* \rightarrow \pi$ transition (Fig. S2†). The fluorescence quantum yield of **In1-NH_2** is 0.033 measured at 350 nm. To confirm the fluorescence stability of **In1-NH_2**, the fluorescence intensity was first measured under different pH conditions. The value reached a maximum at pH = 7, so pH = 7 was chosen for the following experiments (Fig. S3†).

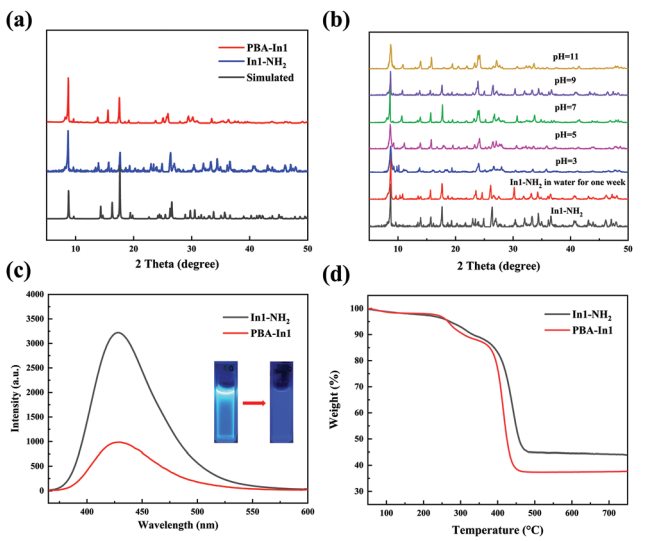

Fig. 2 (a) PXRD patterns of the simulated, as-synthesized **In1-NH_2** and **PBA-In1**; (b) PXRD patterns of **In1-NH_2** and **In1-NH_2** treated with water, various acidic and basic aqueous solutions; (c) fluorescence emission spectra of the **In1-NH_2** and **PBA-In1** composite suspensions under excitation at 350 nm; (d) thermogravimetric curves of **In1-NH_2** and **PBA-In1** composite.

The boronic acid group is a typical functional group for the detection of H_2O_2; thus, CPBA was introduced into **In1-NH_2** *via* a PSM strategy. Through grafting CPBA to **In1-NH_2** with cross-linking agents EDC and NHS, the **PBA-In1** composite with abundant boronic acid sites was prepared (Scheme S1†). Fourier transform infrared spectroscopy (FTIR) indicates that the sharp band of $-NH_2$ (3374 cm^{-1}) in **In1-NH_2** disappears in **PBA-In1** and the peak of –C=O in **PBA-In1** appears at 1683 cm^{-1} (Fig. S4†). The peak at 1052 cm^{-1} is the =C–N stretching band and the B–O stretching vibration is present at 1325 cm^{-1}. The peaks located at 996 cm^{-1} and 1127 cm^{-1} are ascribed to the B–O–H asymmetric stretching band and B–O–H wagging band, respectively.[57–59] These results demonstrate that the CPBA is successfully grafted onto the **In1-NH_2**. Furthermore, X-ray photoelectron spectra (XPS) show the B 1s signal at around 191.0 eV, which confirms that the CPBA is loaded onto the framework (Fig. S5†). For practical applications, stability is an important indicator for evaluating the properties of probe materials. The PXRD patterns show that both the position and relative strength of the major diffraction peaks of **PBA-In1** are consistent with the **In1-NH_2** pattern (Fig. 2a), confirming that the skeleton structure of **In1-NH_2** is not damaged after the PSM process of CPBA. TGA analysis shows that the decomposition temperature of **PBA-In1** composite is close to that of **In1-NH_2**. The **PBA-In1** remains stable until around 485 °C (Fig. 2d).

Fig. S6† reveals the ultraviolet-visible absorption spectra of **In1-NH_2** and the **PBA-In1** composite; the location of the absorption peak of **PBA-In1** shows a slight red shift and the absorption peak intensity increases owing to the improvement of conjugation degree. Compared with **In1-NH_2**, the fluorescence intensity of the **PBA-In1** composite is weaker (λ_{ex} = 350 nm) (Fig. 2c). Because the negative inductive effect of the carbonyl eliminated the partial positive conjugative effect of the amino group, part of the fluorescence signal of the chromophore of benzene was quenched and the fluorescence intensity of **PBA-In1** decreased. The fluorescence quantum yield of **PBA-In1** is 0.016 measured at 350 nm. Since water is an important and indispensable substance in the human

body, accounting for almost 70% of it, the fluorescence stability of **PBA-In1** in water is a concern for practical application requirements. After one week of immersion in water for **PBA-In1**, its fluorescence emission spectrum was measured again. The results show that the fluorescence intensity is hardly changed, indicating the good fluorescence stability of **PBA-In1** in water (Fig. S7†). Acid–base stability tests of **PBA-In1** were also performed and the PXRD patterns were recorded (Fig. S8†). The PXRD patterns at different pH values match precisely, indicating the good stability of **PBA-In1**.

The morphological characteristics of the obtained samples were further revealed by scanning electron microscopy (SEM). **In1-NH$_2$** exhibits a cuboid crystal morphology and, after the PSM process, **PBA-In1** shows similar cuboid morphology and crystal size, as shown in Fig. 3a–c. The EDS mapping images of **PBA-In1** show that each element is homogeneously distributed throughout the 3D framework (Fig. 3e–i). The uniform distribution of B element also indicates that CPBA is successfully bound to **In1-NH$_2$** through the PSM process.

Detection of heavy metal ions

Heavy metal ions are a main factor in water pollution and seriously affect the environment and human health. Considering its unique structure and excellent fluorescence characteristics, **In1-NH$_2$** was tested for detection of heavy metal ions in water. To explore the sensing ability and selectivity for heavy metal ions, the detection potential of **In1-NH$_2$** for different metal cations was studied. MCl_x (1 mM, M = Zn^{2+}, Ca^{2+}, Cd^{2+}, K^+, Ba^{2+}, Mg^{2+}, Na^+, Mn^{2+}, Ni^{2+}, Fe^{3+}, Cu^{2+} and Pb^{2+}) was immersed in 2 mL of uniformly ground **In1-NH$_2$** suspension for subsequent fluorescence measurements (Fig. 4a). In view of the prominent quenching effects of Fe^{3+}, Cu^{2+} and Pb^{2+}, **In1-NH$_2$** is feasible as a fluorescent probe for heavy metal ions as well as for water quality detection (Fig. 4b). The quenching effect shows a short response time: within 10 s. To further investigate the possibility of **In1-NH$_2$** as a fluorescent sensor for Fe^{3+}, Cu^{2+} and Pb^{2+} detection, corresponding metal ion aqueous solutions with different concentrations (0–0.5 mM) were added to a 2 mL **In1-NH$_2$** uniform suspension and the results are displayed in Fig. 5.

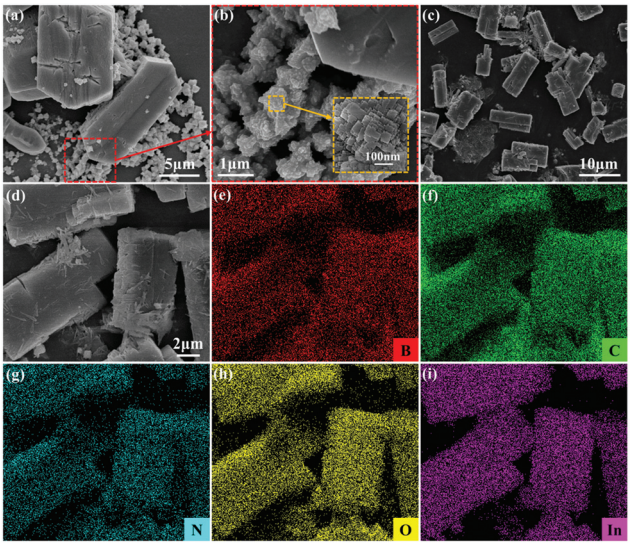

Fig. 3 SEM images of **In1-NH$_2$** (a and b) and **PBA-In1** (c and d); EDS mapping images of **PBA-In1** (e–i).

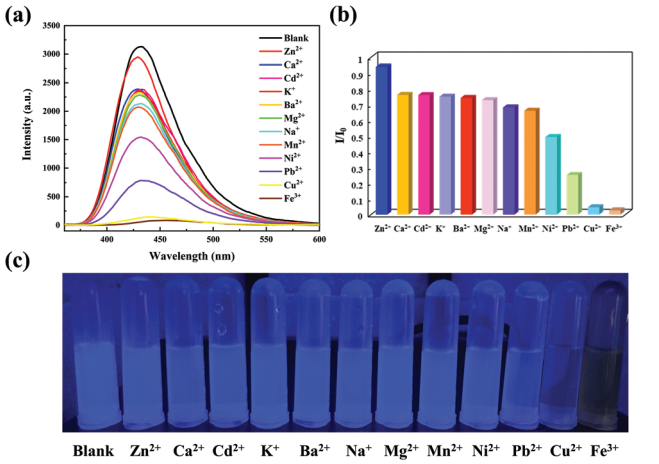

Fig. 4 (a) Fluorescence emission spectra of probe **In1-NH$_2$** in aqueous suspension with different metal ions; (b) fluorescence response histogram of **In1-NH$_2$** suspension towards the relevant species; (c) the corresponding fluorescence images under 365 nm UV light.

With the increase of the concentration of heavy metal ions, the fluorescence emission at 350 nm excitation decreased gradually. Upon the gradual addition of Fe^{3+} to the **In1-NH$_2$** suspension, the fluorescence emission peak shows a slight red shift. The fluorescence calibration curves can be estimated by the Stern–Volmer (SV) equation: $I_0/I = 1 + K_{SV}[C]$. Notably, both Fe^{3+} and Cu^{2+} exhibit outstanding linear correlation within a broad range of 0.01–0.5 mM, while Pb^{2+} only shows a good linear relationship under a narrow concentration range from 0.01 to 0.06 mM. In addition, the LODs based on the standard equation $3\sigma/K$ were calculated to be 0.11 μM for Fe^{3+}, 0.14 μM for Cu^{2+} and 1.15 μM for Pb^{2+} (where K represents the slope of the calibration curve, 3 is the factor at the 99% confidence level and σ represents the standard deviation of replicated blank measurements) (Table S3†). The results were comparable with previously reported research using various detection procedures and demonstrated the feasibility of **In1-NH$_2$** for heavy metal ion detection (Table S5†). To utilize **In1-NH$_2$** practically, competitive experiments were carried out to evaluate its anti-interference ability. Different metal cations (1 mM) were added to the detection systems of Fe^{3+}, Cu^{2+} and Pb^{2+} (0.5 mM) and the results are shown in Fig. S9.† It is obvious that **In1-NH$_2$** shows excellent recognition ability and may be used in actual applications.

Detection of ClO^-

ClO^- is a type of active chlorine commonly used for disinfection and sterilization in water treatment. However, excessive residual ClO^- in water poses a serious threat to human health.

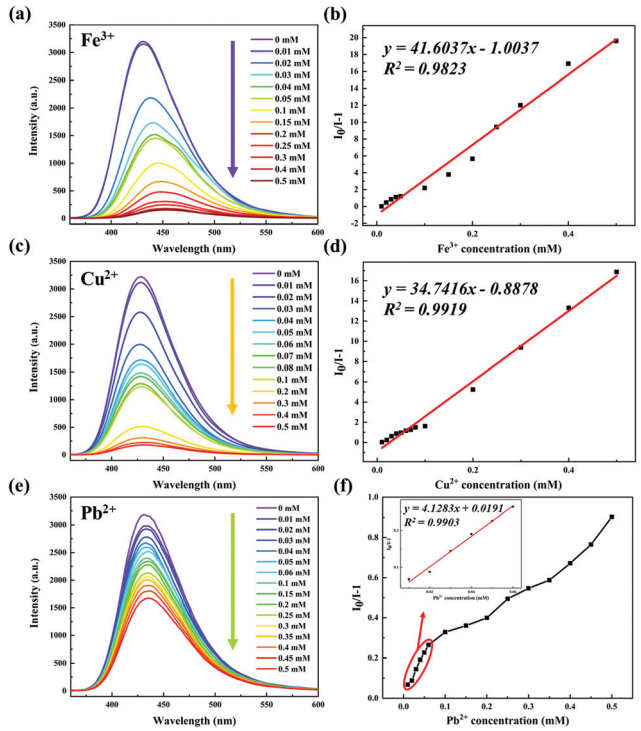

Fig. 5 (a) Emission spectra of **In1-NH$_2$** with different concentrations of Fe^{3+}; (b) the linear relationship between $I_0/I - 1$ and Fe^{3+} concentration in the range of 0–0.5 mM; (c) emission spectra of **In1-NH$_2$** with different concentrations of Cu^{2+}; (d) the linear relationship between $I_0/I - 1$ and Cu^{2+} concentration in the range of 0–0.5 mM; (e) emission spectra of **In1-NH$_2$** with different concentrations of Pb^{2+}; (f) the relationship between $I_0/I - 1$ and Pb^{2+} concentration (inset is the calibration curve for Pb^{2+} detection from 0 to 0.06 mM).

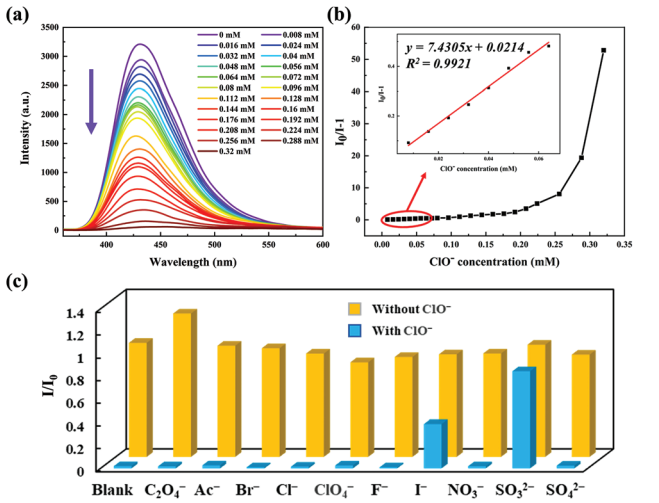

Fig. 6 (a) Emission spectra of probe **In1-NH$_2$** with different concentrations of ClO^-; (b) the relationship between $I_0/I - 1$ and ClO^- concentrations (inset is the calibration curve for ClO^- detection from 0 to 0.064 mM); (c) the anti-interference ability of probe **In1-NH$_2$** towards various interferents.

It is extremely important to develop a reliable low-cost probe for monitoring residual ClO^- in water sources. Considering that the amino groups of **In1-NH$_2$** can act as hydrogen bond donors, possible hydrogen bonding may endow **In1-NH$_2$** with the ability to detect ClO^- in water. As expected, the fluorescence intensity of **In1-NH$_2$** was significantly quenched after the introduction of ClO^-. The response time of **In1-NH$_2$** to ClO^- was studied first. As shown in Fig. S10,† the fluorescence was quenched absolutely within one minute, so one minute was chosen for subsequent experiments. The fluorescence intensity of **In1-NH$_2$** was recorded with the ClO^- concentration ranging from 0 to 0.32 mM. As illustrated in Fig. 6a, with the increasing concentration of ClO^-, the fluorescence intensity of **In1-NH$_2$** gradually decreased. The fluorescence intensity shows an excellent linear relationship with the concentration of ClO^- from 0 to 0.064 mM (Fig. 6b). The Stern–Volmer (SV) equation was expressed as $I = 7.4305C + 0.0214$ with a correlation coefficient (R^2) of 0.9921. On the basis of $3\sigma/K$, the LOD was calculated to be 0.64 μM. Compared with other reported sensors of ClO^-, **In1-NH$_2$** exhibits good sensitivity, LOD and response time (Table S6†).

Usually, the water environment is sophisticated and varied. Therefore, the selectivity of **In1-NH$_2$** towards ClO^- was further tested. Different competitive anions (1 mM, including $C_2O_4^{2-}$, CH_3COO^-, Br^-, Cl^-, F^-, I^-, ClO_4^-, NO_3^-, SO_3^{2-} and SO_4^{2-}) were introduced into **In1-NH$_2$** aqueous suspensions, followed by the addition of ClO^- solution (0.32 mM). As expected, the fluorescence of **In1-NH$_2$** could not be quenched by these competitive anions (Fig. S11†), but with the introduction of ClO^-, the fluorescence emission was almost quenched completely, except for with SO_3^{2-} and I^- (Fig. 6c). That is due to the reducibility of SO_3^{2-} and I^-, which cannot coexist with ClO^-. In general, all the results demonstrate the high selectivity of **In1-NH$_2$** towards ClO^-.

Detection of H_2O_2

H_2O_2, as a versatile biomarker, has crucial effects which can reflect human health and its detection is of high significance. In view of the characteristic nucleophilic reaction between the boronic acid group and H_2O_2, the fluorescence spectra of **PBA-In1** in HEPES solution were recorded before and after the addition of H_2O_2. As shown in Fig. S12,† the response time of **PBA-In1** in the presence of H_2O_2 was tested first. 25 μM of H_2O_2 was added into the **PBA-In1** suspension and a time-dependent fluorescence measurement was conducted every 5 minutes. After 30 minutes of reaction, the fluorescence response of **PBA-In1** changed slowly and came to saturation. Therefore, 30 minutes was chosen as the optimal response time between H_2O_2 and **PBA-In1** in subsequent experiments.

To further investigate the sensitivity of **PBA-In1** as a fluorescent sensor for H_2O_2 detection, different concentrations of H_2O_2 from 0 to 80 μM were added to the uniform **PBA-In1** suspension and the corresponding fluorescence spectra were recorded 30 minutes later. As shown in Fig. 7a, the emission intensity of **PBA-In1** at 429 nm increases asymptotically with the gradual increase of H_2O_2 concentration upon 350 nm exci-

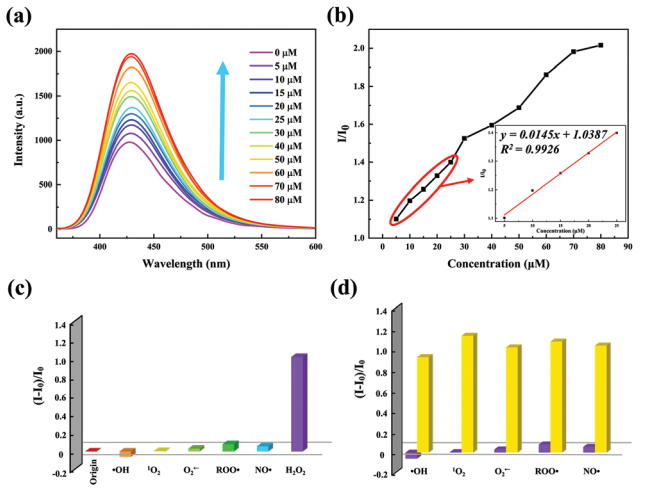

Fig. 7 (a) Emission spectra of probe **PBA-In1** with different H_2O_2 concentrations; (b) the linear relationship between I_{429} and H_2O_2 concentration in the range of 0–80 μM; (c) the selectivity of probe **PBA-In1** against the relevant species; (d) the anti-interference ability of probe **PBA-In1** against the relevant species.

tation. In addition, a good linear relationship was observed between the fluorescence intensity and the H_2O_2 concentrations in the range of 0–25 μM (Fig. 7b). The calibration curve can be fitted to $I = 0.0145C + 1.0387$, where the correlation coefficient (R^2) is 0.9926 and K is estimated at 1.45×10^4 M^{-1}. The LOD is 0.42 μM based on the standard relation $3\sigma/K$ (Table S4†) and is superior to previously reported H_2O_2 sensing materials using various detection procedures (Table S7†). The fluorescence test confirmed the possibility of detecting H_2O_2 concentration with **PBA-In1**.

To explore the specific fluorescence response of the sensor to H_2O_2, the interference of other substances with the fluorescence performance of **PBA-In1** should be considered. Therefore, the fluorescence response of **PBA-In1** to various interferents (including $^{\bullet}OH$, $^1O_2$, $O_2^{\bullet-}$, $ROO^{\bullet}$ and $NO^{\bullet}$) was investigated under the same conditions as those of H_2O_2 detection (Fig. S13†). As expected, the fluorescence of **PBA-In1** was greatly enhanced only in the presence of H_2O_2. In contrast, the fluorescence intensity does not change significantly after the addition of other competitive components due to the unique nucleophilic interaction between H_2O_2 and the boronic acid group (Fig. 7c). Usually, since some co-existing substances may disturb the detection of H_2O_2, it is necessary to effectively identify the target analyte in the presence of other co-existing analytes. By adding different competitive analytes into the **PBA-In1** suspension treated with H_2O_2, anti-interference experiments were carried out to investigate the H_2O_2 detection practicality of **PBA-In1**. As shown in Fig. 7d, the fluorescence enhancement of **PBA-In1** caused by H_2O_2 was not influenced by other components, illustrating the high selectivity and good anti-interference ability of **PBA-In1** for the detection of H_2O_2. Despite other fluorescent H_2O_2 detection materials having been reported, they are still subject to some potential restrictions, such as some probes with enzymes that usually need harsh reaction conditions.[60,61] The sulfonic ester hydrolysis reaction for H_2O_2 detection may lack specificity and the synthesis of some organic fluorescent H_2O_2 probes may be complicated.[62,63] In comparison, **PBA-In1** can avoid these limitations and has a promising prospect.

Sensing mechanism

To determine a plausible sensing mechanism for **In1-NH$_2$** with heavy metal ions (Fe^{3+}, Cu^{2+} and Pb^{2+}) and ClO^-, systematic research was conducted. As shown in Fig. S14,† the main diffraction peaks of **In1-NH$_2$** remain stable after the detection of heavy metal ions and ClO^-, which demonstrates that the observed fluorescence quenching is not caused by framework collapse. Subsequently, the competitive adsorption mechanism was investigated. The excitation band of **In1-NH$_2$** shows a significant overlap with the ultraviolet absorption bands of Fe^{3+} and ClO^- in the range of 250–400 nm, which indicates the existence of competitive adsorption. Also, part of the excitation energy is absorbed by Fe^{3+} and ClO^-, resulting in a fluorescence quenching effect. For Cu^{2+} and Pb^{2+}, no competitive adsorption contributes to the fluorescence response (Fig. S15†). The response time for heavy metal ions is extremely short (within 10 s), excluding the possibility of ion exchange.

In addition, for heavy metal ion detection, host–guest interaction may be the main reason for the fluorescence quenching phenomenon. The ligand of **In1-NH$_2$** may act as the electron donor, while Fe^{3+}, Cu^{2+} and Pb^{2+}, with unsaturated electron configurations, can behave as ideal electron acceptors. When the heavy metal ions coordinate with the amino groups of **In1-NH$_2$**, the excited state electrons of the conduction band of **In1-NH$_2$** can easily transfer to the unfilled 3d orbitals of Fe^{3+} and Cu^{2+} and 6p orbitals of Pb^{2+}. Thus, electron transfer may be a reasonable explanation for the fluorescence quenching of **In1-NH$_2$**. The above conjecture is confirmed by the XPS in Fig. 8. The N 1s spectrum of **In1-NH$_2$** can be decomposed into two peaks at the binding energies of 399.6 eV and 399.0 eV which are attributed to the nitrogen in C–N– and –NH_2, respectively. After the detection of Fe^{3+}, Cu^{2+} and Pb^{2+}, significant shifts of the two fitted peaks were observed and are ascribed to the chelation between the heavy metal ions and the amino groups. After the detection of Fe^{3+}, Cu^{2+} and Pb^{2+}, the zeta potential values of **In1-NH$_2$** increased from −10.79 mV to 35.34 mV, 0.07 mV and 0.45 mV, respectively, indicating electrostatic interaction between **In1-NH$_2$** and the heavy metal ions, which may cause electron transfer. Fluorescence lifetime decay experiments were performed in the absence and presence of heavy metal ions and the data were fitted by a two exponential decay function. The fluorescence lifetime of the original **In1-NH$_2$** suspension is 22.44 μs which decreases to 17.74 μs, 15.33 μs and 16.39 μs with the addition of Fe^{3+}, Cu^{2+} and Pb^{2+}, respectively, indicating that the fluorescence quenching effect involves the dynamic quenching mechanism (Fig. S16†). However, the change in the fluorescence lifetime is not obvious, confirming that static quenching is dominant. The

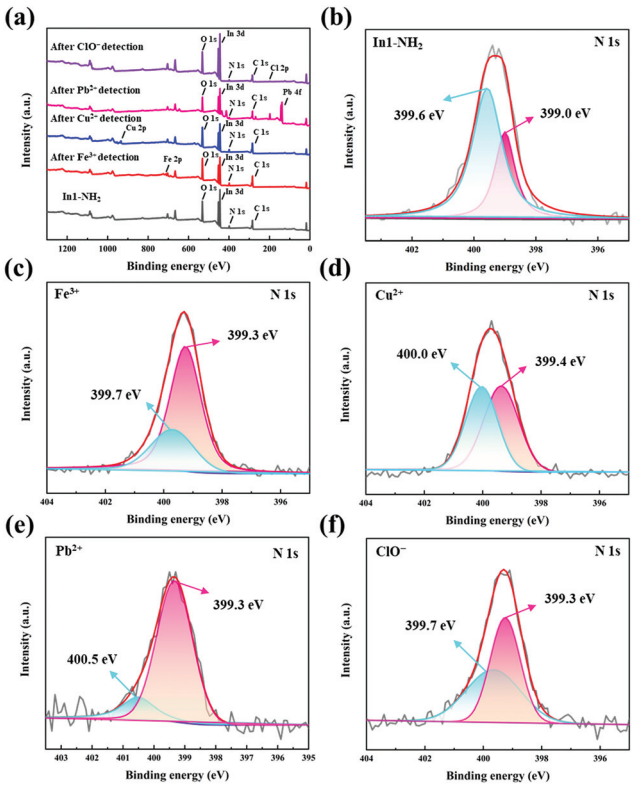

Fig. 8 (a) XPS spectra of **In1-NH$_2$** before and after detection; (b) the N 1s spectra of **In1-NH$_2$**; (c) the N 1s spectra of **In1-NH$_2$** after the detection of Fe^{3+}; (d) the N 1s spectra of **In1-NH$_2$** after the detection of Cu^{2+}; (e) the N 1s spectra of **In1-NH$_2$** after the detection of Pb^{2+}; (f) the N 1s spectra of **In1-NH$_2$** after the detection of ClO^-.

mechanism of fluorescence quenching is mainly a combination of dynamic and static quenching. In conclusion, the fluorescence quenching mechanisms for heavy metal ions might be attributed to the synergistic reaction of competitive absorption and electron transfer.

To investigate the mechanism of ClO^- detection, further tests were conducted. It is well known that the amino group can serve as a binding site for ions.[64] Considering the active amino groups of **In1-NH$_2$**, there might be hydrogen bond interactions between **In1-NH$_2$** and ClO^-. The suitable pore structure and excellent porosity of **In1-NH$_2$** can also pre-concentrate analytes to achieve efficient fluorescence detection. The ClO^- ions are absorbed on the surface of **In1-NH$_2$** or into **In1-NH$_2$** through the channels of the framework, shortening the distance between the amino group and ClO^- and forming the N–H···O–Cl hydrogen bond. As verified in Fig. 8f, the N 1s binding energy of **In1-NH$_2$** increased after the detection of ClO^-. The hydrogen bond can act as a bridge for electron exchange and promote the energy transfer between **In1-NH$_2$** and ClO^- which triggers the fluorescence quenching phenomenon. The fluorescent lifetime of the original **In1-NH$_2$** suspension decayed from 22.44 μs to 16.42 μs, also demonstrating the existence of a dynamic quenching mechanism (Fig. S16†). The inconspicuous change in fluorescence lifetime indicates the dominance of static quenching, though the quenching effect of **In1-NH$_2$** with ClO^- involves both static and dynamic quenching.

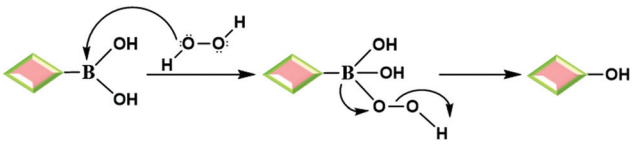

Scheme 2 Mechanism for the fluorescence behavior of **PBA-In1** in the presence of H_2O_2.

The mechanism of detecting H_2O_2 with **PBA-In1** was explored. First, after grafting the 4-carboxyl phenylboronic acid to **In1-NH$_2$**, the negative inductive effect of the carbonyl eliminated part of the positive conjugative effect of the amino, thus partially quenching the fluorescence of **In1-NH$_2$**. With the addition of H_2O_2, the fluorescence intensity of **PBA-In1** showed an obvious increase. H_2O_2 is a good nucleophile due to the α-effect of the adjacent non-bonding orbitals on its oxygen atoms.[65,66] As an electron-deficient group, the boronic acid group can react with H_2O_2 and then undergo chemoselective oxidative cleavage to generate an electron-rich phenol group (mechanism shown in Scheme 2). Hence, the fluorescence was enhanced, showing a strong emission signal. It is worth mentioning that the PXRD of **PBA-In1** did not significantly change after the detection of H_2O_2 (Fig. S17†), which demonstrates that the structural integrity of the employed MOF was not damaged after the reaction with H_2O_2. The result can also be confirmed by the FTIR analysis: the B–O bond of **PBA-In1** disappeared at 1325 cm^{-1} and, at the same time, the peaks of the phenol hydroxyl group at 3443 cm^{-1} and 1204 cm^{-1} were observed after the reaction with H_2O_2 (Fig. S4†). FTIR results provide direct support for the transformation from boronic acid groups to hydroxyl groups. Further, the XPS spectra clearly indicate the mechanism, showing a decrease of the B element in **PBA-In1** (Fig. S5†). Taking into account the detection mechanism of **PBA-In1** for hydrogen peroxide, fluorescent probes were prepared through mixed functionalization strategies and are expected to be an effective means to monitor the formation of metabolites during human metabolism. For example, hydrogen peroxide can be produced in the process of electron transport in the respiratory chain in humans; glucose also produces hydrogen peroxide under the action of glucose oxidase.

Conclusions

In summary, we successfully designed a mixed-functionalization strategy on In-MOF for water quality monitoring and biomarker detection. Based on the specific fluorescence quenching response of **In1-NH$_2$** to heavy metal ions and ClO^-, rapid quantitative fluorescence detection of heavy metal ions (the LOD is 0.11 μM for Fe^{3+}, 0.14 μM for Cu^{2+}, 1.15 μM for Pb^{2+}) and ClO^- (LOD is 0.64 μM) in aqueous solution is rea-

lized. Furthermore, **In1-NH$_2$** was functionalized with phenylboronic acid *via* a PSM strategy to realize the detection of H_2O_2. On account of the nucleophilic reaction between H_2O_2 and the boronic acid group, **PBA-In1** shows excellent fluorescence turn-on behavior to H_2O_2. The probe exhibits good sensitivity to H_2O_2 in HEPES buffer with a LOD of 0.42 μM. The presented strategy is feasible, simple and superior in selectivity and sensitivity. Therefore, **In1-NH$_2$** and **PBA-In1** show great prospects for applications in multi-functional detection and analysis.

Conflicts of interest

There are no conflicts of interest to declare.

Acknowledgements

This work was supported by National Natural Science Foundation of China (Grant No. 21873025, 22072034 and 22001050). We also like to thank the referees for their constructive comments.

Notes and references

1 O. Zadorozhnaya, D. Kirsanov, I. Buzhinsky, F. Tsarev, N. Abramova, A. Bratov, F. J. Muñoz, J. Ribó, J. Bori, M. C. Riva and A. Legin, *Sens. Actuators, B*, 2015, **207**, 1069–1075.
2 X. Yang, Y. Zhang, P. Zhang, N. He, Q. Yang, H. Peng, B. Zhai and J. Gui, *Sens. Actuators, B*, 2018, **267**, 608–616.
3 P. Halkare, N. Punjabi, J. Wangchuk, A. Nair, K. Kondabagil and S. Mukherji, *Sens. Actuators, B*, 2019, **281**, 643–651.
4 X. Fang, Z. Zeng, Q. Li, Y. Liu, W. Chu, T. Maiyalagan and S. Mao, *Sens. Actuators, B*, 2021, **332**, 129526.
5 M. A. Shenashen, S. A. El-Safty and E. A. Elshehy, *J. Hazard. Mater.*, 2013, **260**, 833–843.
6 H. Qi, M. Teng, M. Liu, S. Liu, J. Li, H. Yu, C. Teng, Z. Huang, H. Liu, Q. Shao, A. Umar, T. Ding, Q. Gao and Z. Guo, *J. Colloid Interface Sci.*, 2019, **539**, 332–341.
7 Y. Han, X. Wu, X. Zhang, Z. Zhou and C. Lu, *ACS Sustainable Chem. Eng.*, 2016, **4**, 5667–5673.
8 F.-Y. Ge, G.-H. Sun, L. Meng, S.-S. Ren and H.-G. Zheng, *Cryst. Growth Des.*, 2019, **20**, 1898–1904.
9 P. Jia, Z. Wang, Y. Zhang, D. Zhang, W. Gao, Y. Su, Y. Li and C. Yang, *Spectrochim. Acta, Part A*, 2020, **230**, 118084.
10 S. A. El-Safty, M. Khairy and M. Ismael, *Sens. Actuators, B*, 2012, **166–167**, 253–263.
11 B. Gu, M. Ye, L. Nie, Y. Fang, Z. Wang, X. Zhang, H. Zhang, Y. Zhou and Q. Zhang, *ACS Appl. Mater. Interfaces*, 2018, **10**, 1028–1032.
12 J. J. Lee, Y. W. Choi, G. R. You, S. Y. Lee and C. Kim, *Dalton Trans.*, 2015, **44**, 13305–13314.
13 Y. Su, D. Zhang, P. Jia, W. Gao, Y. Li, J. He, C. Wang, X. Zheng, Q. Yang and C. Yang, *Eur. Polym. J.*, 2019, **112**, 461–465.
14 S. Zhang, M. Xiao, Y. Zhang, Y. Li, H. Liu, G. Han, B. Rathi, K. Lyu and L. Wu, *Anal. Chim. Acta*, 2020, **1105**, 208–213.
15 C. Wang, J. Wu, K. Jiang, M. G. Humphrey and C. Zhang, *Sens. Actuators, B*, 2017, **238**, 1136–1143.
16 Z. Yuan, M. Peng, Y. He and E. S. Yeung, *Chem. Commun.*, 2011, **47**, 11981–11983.
17 Y. Su, D. Zhang, P. Jia, W. Gao, Y. Li, Z. Bai, X. Liu, Q. Deng, J. Xu and C. Yang, *Spectrochim. Acta, Part A*, 2019, **217**, 86–92.
18 B. Wang, D. Chen, S. Kambam, F. Wang, Y. Wang, W. Zhang, J. Yin, H. Chen and X. Chen, *Dyes Pigm.*, 2015, **120**, 22–29.
19 C. Chang, F. Wang, J. Qiang, Z. Zhang, Y. Chen, W. Zhang, Y. Wang and X. Chen, *Sens. Actuators, B*, 2017, **243**, 22–28.
20 J. J. Hu, N. K. Wong, M. Y. Lu, X. Chen, S. Ye, A. Q. Zhao, P. Gao, R. Y. T. Kao, J. Shen and D. Yang, *Chem. Sci.*, 2016, **7**, 2094–2099.
21 J. Boonstra and J. A. Post, *Gene*, 2004, **337**, 1–13.
22 T. L. V. Hoek, L. B. Becker and Z. Shao, *J. Biol. Chem.*, 1998, **273**, 18092–18098.
23 L. C. Lo and C. Y. Chu, *Chem. Commun.*, 2003, **21**, 2728–2729.
24 M. P. Murphy, A. Holmgren, N. G. Larsson, B. Halliwell, C. J. Chang, B. Kalyanaraman, S. G. Rhee, P. J. Thornalley, L. Partridge, D. Gems, T. Nystrom, V. Belousov, P. T. Schumacker and C. C. Winterbourn, *Cell Metab.*, 2011, **13**, 361–366.
25 H. Dai, W. Lu, X. Zuo, Q. Zhu, C. Pan, X. Niu, J. Liu, H. Chen and X. Chen, *Biosens. Bioelectron.*, 2017, **95**, 131–137.
26 Z. Wu, L.-P. Sun, Z. Zhou, Q. Li, L.-H. Huo and H. Zhao, *Sens. Actuators, B*, 2018, **276**, 142–149.
27 S. Toyokuni, K. Okamoto, J. Yodoib and H. Hiai, *FEBS Lett.*, 1995, **358**, 1–3.
28 X. Sun, S. Y. Xu, S. E. Flower, J. S. Fossey, X. Qian and T. D. James, *Chem. Commun.*, 2013, **49**, 8311–8313.
29 V. Carroll, B. W. Michel, J. Blecha, H. VanBrocklin, K. Keshari, D. Wilson and C. J. Chang, *J. Am. Chem. Soc.*, 2014, **136**, 14742–14745.
30 H. Fang, G. Kaur and B. Wang, *J. Fluoresc.*, 2004, **14**, 481–489.
31 B. C. Dickinson, C. Huynh and C. J. Chang, *J. Am. Chem. Soc.*, 2010, **132**, 5906–5915.
32 K. Wannajuk, M. Jamkatoke, T. Tuntulani and B. Tomapatanaget, *Tetrahedron*, 2012, **68**, 8899–8904.
33 C. Wu, Y. Liang, Q. Zhao, Y. Qu, S. Zhang, Q. Wu, Z. Liang, L. Zhang and Y. Zhang, *Chemistry*, 2014, **20**, 8737–8743.
34 H. Yue, X. Bu, M. H. Huang, J. Young and T. Raglione, *Int. J. Pharm.*, 2009, **375**, 33–40.
35 C. Chen, D. Xiong, M. Gu, C. Lu, F. Y. Yi and X. Ma, *ACS Appl. Mater. Interfaces*, 2020, **12**, 35365–35374.

36 D. Feng, P. Li, X. Tan, Y. Wu, F. Wei, F. Du, C. Ai, Y. Luo, Q. Chen and H. Han, *Anal. Chim. Acta*, 2020, **1100**, 232–239.
37 L. Sun, Y. Ding, Y. Jiang and Q. Liu, *Sens. Actuators, B*, 2017, **239**, 848–856.
38 L. Huang, X. Zhang and Z. Zhang, *Anal. Chim. Acta*, 2018, **1044**, 119–130.
39 M. Sk, S. Banesh, V. Trivedi and S. Biswas, *Inorg. Chem.*, 2018, **57**, 14574–14581.
40 S. Xu, A. C. Sedgwick, S. A. Elfeky, W. Chen, A. S. Jones, G. T. Williams, A. T. A. Jenkins, S. D. Bull, J. S. Fossey and T. D. James, *Front. Chem. Sci. Eng.*, 2019, **14**, 112–116.
41 L. Guo, Y. Liu, F. Qu, Z. Liu, R. Kong, G. Chen, W. Fan and L. Xia, *Mikrochim. Acta*, 2019, **186**, 740.
42 C. Yang, J. Xu, J. Li, M. Lu, Y. Li and X. Wang, *Sens. Actuators, B*, 2014, **196**, 133–139.
43 S. Qu, Z. Li and Q. Jia, *ACS Appl. Mater. Interfaces*, 2019, **11**, 34196–34202.
44 T. Sun, P. Wang, R. Fan, W. Chen, S. Hao and Y. Yang, *J. Mater. Chem. C*, 2019, **7**, 3598–3606.
45 D. Sarkar, M. Chowdhury and P. K. Das, *J. Mater. Chem. B*, 2021, **9**, 494–507.
46 Y. Su, J. Yu, Y. Li, S. F. Z. Phua, G. Liu, W. Q. Lim, X. Yang, R. Ganguly, C. Dang, C. Yang and Y. Zhao, *Commun. Chem.*, 2018, **1**, 1–13.
47 R. Goswami, S. C. Mandal, B. Pathak and S. Neogi, *ACS Appl. Mater. Interfaces*, 2019, **11**, 9042–9053.
48 D. Feng, Z. Y. Gu, J. R. Li, H. L. Jiang, Z. Wei and H. C. Zhou, *Angew. Chem., Int. Ed.*, 2012, **51**, 10307–10310.
49 M. Li, D. Xia, Y. Yang, X. Du, G. Dong, A. Jiang and R. Fan, *Adv. Energy Mater.*, 2018, **8**, 1702052.
50 J. Zheng, X. Cui, Q. Yang, Q. Ren, Y. Yang and H. Xing, *Chem. Eng. J.*, 2018, **354**, 1075–1082.
51 J. Li, S. Yuan, J. S. Qin, J. Pang, P. Zhang, Y. Zhang, Y. Huang, H. F. Drake, W. R. Liu and H. C. Zhou, *Angew. Chem.*, 2020, **59**, 9319–9323.
52 J.-N. Hao and B. Yan, *Adv. Funct. Mater.*, 2017, **27**, 1603856.
53 R. J. Marshall, S. L. Griffin, C. Wilson and R. S. Forgan, *J. Am. Chem. Soc.*, 2015, **137**, 9527–9530.
54 X. Zheng, R. Fan, Y. Song, A. Wang, K. Xing, X. Du, P. Wang and Y. Yang, *J. Mater. Chem. C*, 2017, **5**, 9943–9951.
55 H. Hintz and S. Wuttke, *Chem. Mater.*, 2014, **26**, 6722–6728.
56 V. K. Maka, P. Tamuly, S. Jindal and J. N. Moorthy, *Appl. Mater. Today*, 2020, **19**, 100613.
57 O. Mansour, I. El Joukhar and S. Belbekhouche, *React. Funct. Polym.*, 2019, **145**, 104377.
58 S. H. Brewer, A. M. Allen, S. E. Lappi, T. L. Chasse, K. A. Briggman, C. B. Gorman and S. Franzen, *Langmuir*, 2004, **20**, 5512–5520.
59 S. Saleem, M. S. Sajid, D. Hussain, F. Jabeen, M. Najam-Ul-Haq and A. Saeed, *Anal. Bioanal. Chem.*, 2020, **412**, 1509–1520.
60 F. Wen, Y. Dong, L. Feng, S. Wang, S. Zhang and X. Zhang, *Anal. Chem.*, 2011, **83**, 1193–1196.
61 X. Chen, G. Wu, Z. Cai, M. Oyama and X. Chen, *Microchim. Acta*, 2013, **181**, 689–705.
62 H. M. K. Yamamoto, Y. Nomura, I. Kohno, L. Hafsi, N. Ueda, S. Yoshida, M. Fukuda, Y. Fukuyasu, Y. Yamauchi and N. Itoh, *J. Am. Chem. Soc.*, 2005, **127**, 68–69.
63 J. Han, C. Chu, G. Cao, W. Mao, S. Wang, Z. Zhao, M. Gao, H. Ye and X. Xu, *Bioorg. Chem.*, 2018, **81**, 362–366.
64 Z. Xiang, C. Fang, S. Leng and D. Cao, *J. Mater. Chem. A*, 2014, **2**, 7662–7665.
65 Y. Ren and H. Yamataka, *J. Org. Chem.*, 2007, **72**, 5660–5667.
66 A. R. Lippert, G. C. Van de Bittner and C. J. Chang, *Acc. Chem. Res.*, 2011, **44**, 793–804.